

Photoluminescence Enhancement of PEG-Modified YAG:Ce³⁺ Nanocrystal Phosphor Prepared by Glycothermal Method

Ryo Kasuya and Tetsuhiko Isobe*

Department of Applied Chemistry, Faculty of Science and Technology, Keio University, 3-14-1 Hiyoshi, Kohoku-ku, Yokohama 223-8522, Japan

Hitoshi Kuma and Junichi Katano

Idemitsu Kosan Co., Ltd., 1280, Kamiizumi, Sodegaura, Chiba 299-0293, Japan

Received: May 25, 2005; In Final Form: September 23, 2005

Y₃Al₅O₁₂:Ce³⁺ (YAG:Ce³⁺) nanocrystals were synthesized in 1,4-butylene glycol (BG) with and without poly(ethylene glycol) (PEG) by the glycothermal method. The internal quantum efficiency of the photoluminescence (PL) corresponding to the 5d → 4f transition of Ce³⁺ in the YAG:Ce³⁺ nanocrystal increased from 21.3 to 37.9% by addition of PEG, while no appreciable change in the primary particle size, the crystallite size, and the lattice distortion was recognized by transmission electron microscopy and X-ray diffractometry. The thermogravimetry–differential thermal analysis, Fourier transform infrared absorption spectroscopy and ¹H → ¹³C cross-polarization magic angle spinning nuclear magnetic resonance (CP-MAS NMR) confirmed the preferential coordination of PEG to the YAG:Ce³⁺ nanocrystal. ²⁷Al single-pulse excitation MAS NMR reveals that the ratio of the 4-fold coordination site to the 6-fold coordination site increased from 0.53 to 0.72 by addition of PEG. We conclude that the surface modification of the YAG:Ce³⁺ nanocrystal by PEG induces the surface passivation, the prevention of the oxidation of Ce³⁺ to Ce⁴⁺, the promotion of the incorporation of Ce³⁺ into YAG and the local structural rearrangement, resulting in the PL enhancement.

1. Introduction

Ce³⁺-doped yttrium aluminum garnet (Y₃Al₅O₁₂), abbreviated as YAG:Ce³⁺, can convert from blue light to green light. YAG:Ce³⁺ phosphor combined with the blue light emitting diode (LED) is applied for the white solid-state LED.¹ Additionally, YAG:Ce³⁺ is applicable for the inorganic electroluminescence display with the light conversion system (Color-By-Blue).²

Generally, the formation of the phase pure YAG from each oxide ingredient by the conventional solid-state reaction requires the high temperatures more than 1100 °C for eliminating several byproducts such as Y₄Al₂O₉ (monoclinic yttrium aluminate, YAM) and YAlO₃ (yttrium aluminum perovskite, YAP).^{3,4} On the contrary, YAG directly crystallizes from the amorphous precursor at the temperature as low as 700 °C in the sol–gel method.⁵ Wet chemical processes, e.g., the hydrothermal method under the supercritical condition and the solvothermal method enable us to obtain the crystalline YAG below 400 °C.^{6,7} Inoue et al. developed the solvothermal method in glycol solvents, called as the glycothermal method. They reported the formation of the phase pure YAG from aluminum compounds and yttrium acetate in 1,4-butylene glycol (1,4-BG).^{8,9}

We have reported that Ce³⁺ ions can be incorporated into the YAG nanocrystal by the glycothermal method.¹⁰ When the YAG:Ce³⁺ nanocrystal phosphor was heated to 1000 °C to burn out the organic species on its surface, the photoluminescence (PL) intensity decreased by a factor of 1/7. This result is entirely opposite to the PL enhancement of the conventional bulk phosphors by heat treatment. We, therefore, focus on the effect

of surface modification by organic species on the PL enhancement of the YAG:Ce³⁺ nanocrystal. Here we report the effect of the surface modifier, poly(ethylene glycol) (PEG), on the chemical interaction and the PL properties for the YAG:Ce³⁺ nanocrystal.

2. Experimental Procedure

Aluminum isopropoxide (12.50 mmol), yttrium(III) acetate tetrahydrate (7.43 mmol), and cerium(III) acetate monohydrate (0.08 mmol) at Ce/(Y + Ce) = 1.0 at. % were suspended in the solvent (52.8 mL) in a glass inner vessel. This vessel was placed in a 120 mL autoclave (Taiatsu Techno Corp., TVS-120-N2). Then, the solvent (10.2 mL) was poured into the gap between the autoclave wall and the vessel. 1,4-BG (HO(CH₂)₄-OH) or the mixture of 1,4-BG and PEG (HO(CH₂CH₂O)_nH; average molecular weight, 190–210) at the volume ratio = 1:1 was used as the solvent. The autoclave was heated to 300 °C at a rate of 3.1 °C/min with stirring at 300 rpm and aged at 300 °C for 2 h. The autogenous pressure gradually increased during autoclave treatment to reach the maximum pressure at the end of aging. After cooling to room temperature, the colloidal solution was washed by ethanol and centrifuged at 10000 rpm for 10 min to obtain the precipitate. After washing and centrifuging repeatedly three times, the precipitate was dried at 50 °C for 1 day to obtain the powder. The samples prepared in 1,4-BG and the mixture of 1,4-BG and PEG are named S(1/0) and S(1/1), respectively.

Crystalline phases were identified by X-ray diffractometry (XRD, Rigaku, Rint 2200), using Cu Kα radiation. The particle morphology and the microstructure were observed by field emission transmission electron microscopy (TEM, Hitachi,

* To whom correspondence should be addressed. E-mail: isobe@aplc.keio.ac.jp.

H-800). The powder sample dispersed in ethanol was dropped on the corrosion mesh and dried under the lamp. The particle size distribution was measured by dynamic light scattering (DLS, Malvern, HPPS), where the as-prepared colloidal solution was diluted in ultrapure water, and the refractive index of bulk YAG, 1.82, was used.

After dissolving the sample in an acidic aqueous solution, the concentrations of Ce, Y, and Al were determined by inductively coupled plasma atomic emission spectroscopy (ICP-AES, Seiko Instruments, SPS-1500VR). Thermogravimetry and differential thermal analysis (TG-DTA, Mac Science, 2020) were carried out in an air flow (200 mL/min) at a heating rate of 10 °C/min. Fourier transform infrared (FT-IR) absorption spectra were measured by a spectrometer (Bio-Rad, Win175) by means of a KBr disk method.

Solid-state ²⁷Al NMR measurements were performed with a Bruker ARX-400 spectrometer operating in a static field of 9.39 T at room temperature. The spectrometer was equipped with a magic angle spinning (MAS) probe head. A zirconia NMR rotor of 4 mm in diameter was spun at 10 kHz. The operating resonance frequencies of proton, aluminum, and carbon were 400.13, 104.26, and 100.62 MHz, respectively. ²⁷Al NMR spectra were measured by the single-pulse excitation (SPE)–MAS with the high-power proton decoupling pulse (radio frequency (ν_{rf}) = 64 kHz). In this measurement, a radio frequency excitation of 40 kHz with the pulse width of 0.62 μ s corresponding to a $\pi/20$ flip angle was used to avoid the selective excitation.¹¹ The recycle delay was 3 s. The Al chemical shift was referenced to the external standard of Al-(H₂O)₆³⁺ (δ = 0 ppm). The ¹H → ¹³C CP-MAS NMR spectra were measured at the contact time, 1 ms, using the pulse width of 3.9 μ s (ν_{rf} = 64 kHz), corresponding to a $\pi/2$ flip angle of ¹H and the high-power proton decoupling pulse (ν_{rf} = 64 kHz). In this measurement, the recycle delay was 4 s. The ¹³C chemical shift was calibrated by using glycine (δ = 43.67 ppm) as an external standard relative to tetramethylsilane (δ = 0 ppm).

Photoluminescence (PL) and its excitation (PLE) spectra were measured by a JASCO FP-6500 spectrometer, where the sample was excited by the blue light with the wavelength of 460 nm. The PL intensity of the sample, relative to that of the bulk (Y_{2.1}-Gd_{0.9})Al₅O₁₂:Ce³⁺ (Kasei Optonix Ltd., P46-Y3) with the internal quantum efficiency of 72% was shown in both spectra. Diffuse reflectance spectra of powder samples were measured by an ultraviolet–visible (UV–vis) optical absorption spectrometer (JASCO, V550), where the white MgO plate was used as a reference standard, and the calibration was carried out using the background at 700 nm.

3. Results

3.1. Structural and Particle Properties. XRD profile (Figure 1) is assigned to the phase pure YAG crystalline structure irrespective of the addition of PEG. TEM images of samples S(1/0) and S(1/1) are shown in Figure 2a,b, respectively. The primary particles of the samples were spherical in shape, and their mean diameter was ca. 10 nm irrespective of the addition of PEG, while the aggregation of the primary particles was more prominent for the sample S(1/1) with PEG. The crystallite size estimated by Scherrer's equation was 22 ± 2 nm for the sample S(1/0); 20 ± 2 nm for the sample S(1/1). The lattice distortion estimated by Wilson's method was $0.2 \pm 0.1\%$ for both samples. The maximum pressure during aging of autoclave treatment was 4.9 MPa for the sample S(1/0) and 1.5 MPa for the sample S(1/1). This difference of the maximum pressure did not affect the crystalline properties of the crystallite size and the lattice

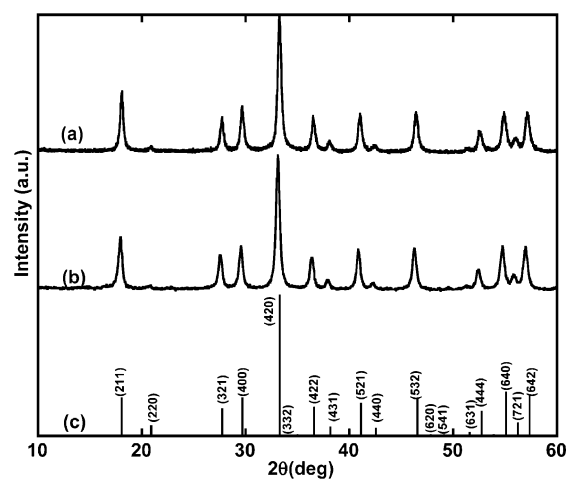


Figure 1. XRD profiles: (a) sample S(1/0), (b) sample S(1/1), and (c) JCPDS card data of YAG (Nos. 33–40).

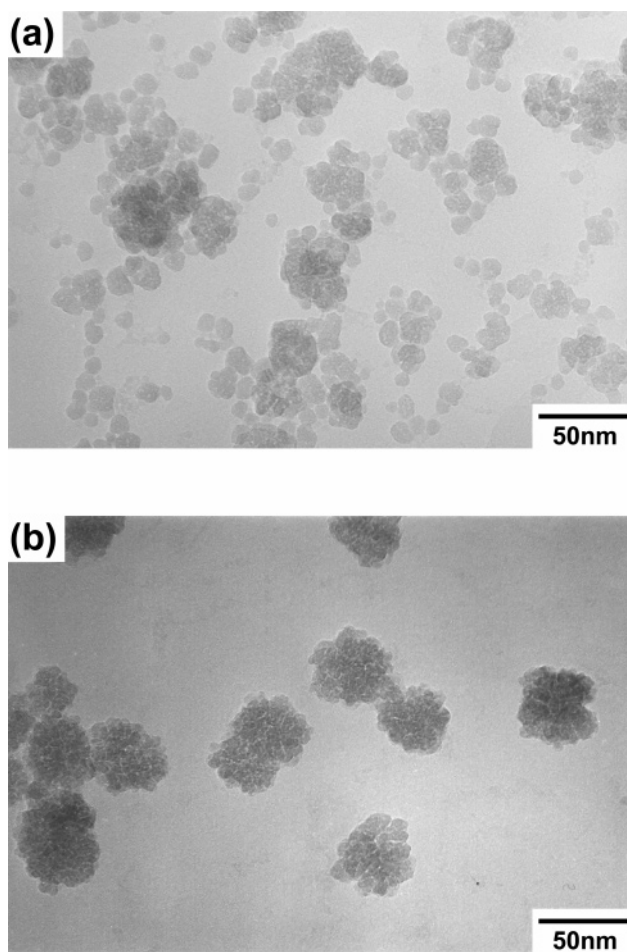


Figure 2. TEM micrographs: (a) sample S(1/0) and (b) sample S(1/1).

distortion. The discrepancy between the primary particle size and the crystallite size appears to be attributed to the crystallographic orientation among the coalescent particles by self-organization, as recognized from the lattice images (not shown).

The compositional analysis by ICP-AES was summarized in Table 1. No appreciable change in the (Y + Ce)/Al ratio was detected irrespective of the addition of PEG, while the Ce/(Ce + Y) ratio of sample S(1/1) is 1.085 times higher than that of sample S(1/0).

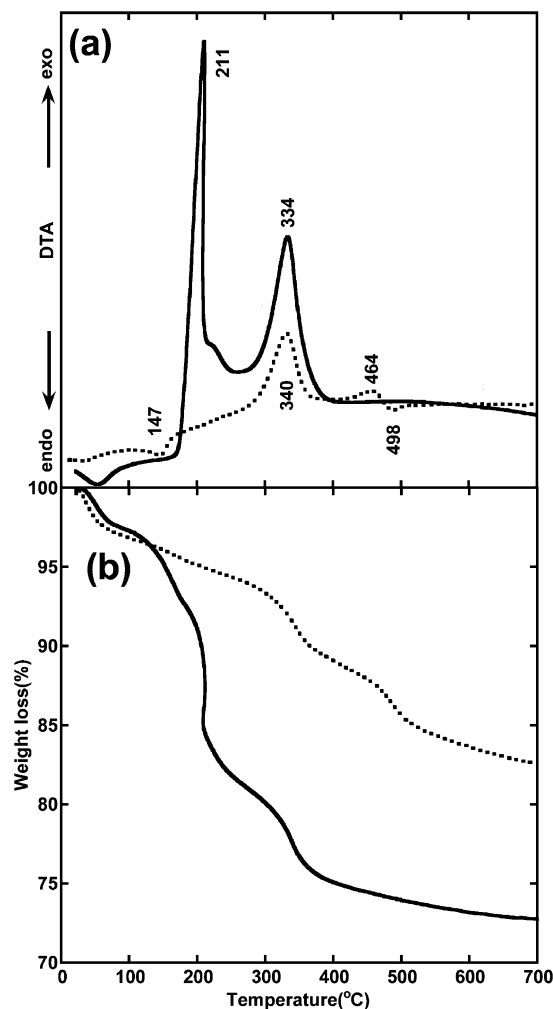


Figure 3. TG-DTA profiles of samples S(1/0) (dashed line) and S(1/1) (solid line): (a) DTA and (b) TG.

TABLE 1: Results of Elemental Analysis Measured by ICP-AES

sample	Ce/(Ce + Y)(at. %)	(Y + Ce)/Al (molar ratio)
S(1/0)	0.94	0.58
S(1/1)	1.02	0.59
nominal	1.00	0.60

3.2. Thermal Behavior. The endothermic peaks at 147 and 498 °C and the exothermic peaks at 340 and 464 °C were observed in the DTA profile of sample S(1/0), as shown by the dashed line in Figure 3a. The endothermic peak at 147 °C is possibly attributed to the vaporization of physisorbed water and ethanol, and the exothermic peak at 340 °C is probably due to the combustion of chemisorbed species such as 1,4-BG and acetate derived from the starting ingredients. Two peaks at 464 (exothermic) and 498 °C (endothermic) might be associated with the structural change accompanied with the weight loss, as referred to the thermal behavior of the alkyl derivatives of boehmite.¹²

The exothermic peak at 211 °C was observed in the DTA profile of sample S(1/1), as shown by the solid line in Figure 3a. This is attributed to the combustion of PEG or the loosely bound acetate (discussed in section 3.3). The exothermic peak shifted from 340 to 334 °C after addition of PEG. Any significant peaks were not observed at temperatures > 400 °C. The weight loss shown in the TG profile (Figure 3b) was accompanied with the endothermic or exothermic reaction shown in the DTA profile. The total weight loss up to 700 °C

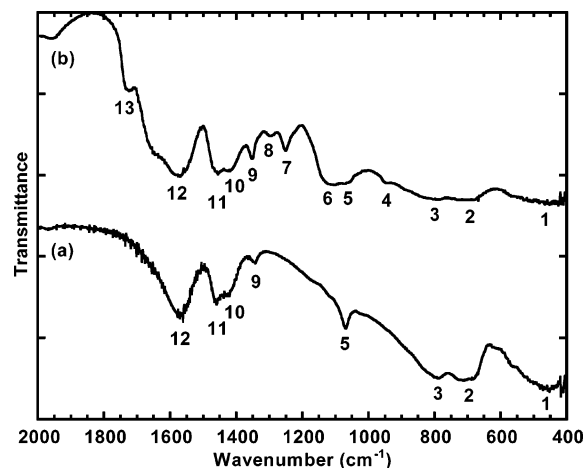


Figure 4. FT-IR spectra: (a) sample S(1/0) and (b) sample S(1/1).

TABLE 2: Assignments of FT-IR Spectra for Samples S(1/0) and S(1/1)

peak no.	S(1/0) (cm ⁻¹)	S(1/1) (cm ⁻¹)	assignment ^a	ref
1	~450	~450	$\nu(\text{Al}-\text{O})$ for AlO_6	13
2	~700	~700	$\nu(\text{Al}-\text{O})$ for AlO_4	13
3	790	790	$\nu(\text{Al}-\text{O})$ for AlO_4	13
4		945	$\nu(\text{CH}_2)$, $\nu(\text{CH}_3)$	14
5	1070	1070	$\nu(\text{C}-\text{O})$	14
6		1110	$\nu(\text{C}-\text{O})$, $\nu(\text{C}-\text{C})$	14
7		1250	$\nu(\text{CH}_2)$	14
8		1295	$\nu(\text{CH}_2)$	14
9		1350	$\nu(\text{CH}_3)$	14
10	1430	1420	$\nu^s(\text{COO})$	14, 15
11	1460	1455	$\nu^s(\text{CH}_2)$	14
12	1560	1570	$\nu^a(\text{COO})$	14, 15
13		1725	$\nu(\text{C}=\text{O})$	14

^a ν , stretching; r, rocking; t, twisting; w, wagging; sr, scissoring; a, asymmetric mode; s, symmetric mode.

increased from 17.4 wt % (sample S(1/0)) to 27.3 wt % (sample S(1/1)) by addition of PEG.

3.3. Identification of Adsorbed Chemical Species. Figure 4 shows FT-IR spectra of samples S(1/0) and S(1/1). The peak positions and the assignments were given in Table 2. The peaks at ~1425 and ~1565 cm⁻¹ are assigned to the symmetric and asymmetric modes of carboxyl groups derived from the starting ingredients, respectively.¹⁵ These are characteristic of carboxyl groups coordinated to metal ions on the surface of the particles. Additional peaks corresponding to PEG were observed in the FT-IR spectrum of sample S(1/1). We also note the appearance of the peak at 1725 cm⁻¹ due to free carbonyl groups. This indicates that the oxygen atoms of PEG are coordinated to the metal ions of YAG:Ce³⁺ nanocrystals more preferentially than those of carbonyl groups.

Figure 5 shows ¹H → ¹³C CP-MAS NMR spectra of samples S(1/0) and S(1/1). The chemical shifts were summarized in Table 3. Most of peaks for sample S(1/0) were identified as 1,4-BG and carboxyl groups derived from starting ingredients.¹⁶ The peak around 180 ppm is assigned to carboxyl groups coordinated to metal ions on the surface of the particles.¹⁵ This is consistent with the above-mentioned FT-IR result. The broad peak around 130 ppm originates from the polyimide of the rotor. Additional two ¹³C NMR peaks were observed at 71.3 and 73.1 ppm in the spectrum of sample S(1/1). On the basis of the chemical shifts of tetraethylene glycol calculated by ChemDraw (Cambridge Soft Co.) shown in Table 3, these peaks are identified with the repeated unit (-OCH₂CH₂-) and the end group (HOCH₂CH₂-) in PEG. The chemical interaction of PEG with the YAG:Ce³⁺ nanocrystal is consistent with the above-

TABLE 3: Assignment of ¹H → ¹³C CP-MAS NMR Spectra

peak no.	shift (ppm)				assignment
	S(1/0)	S(1/1)	AC ^a	1,4-BG ^a	
1	24.1	25.2	20.8		C*H ₃ -COO-Metal
2	29	30		29.2	HO-CH ₂ -C*H ₂ -C*H ₂ -CH ₂ -OH
3	61.7	62.2		60.9	{ HO-C*H ₂ -CH ₂ -CH ₂ -C*H ₂ -OH HO-C*H ₂ -CH ₂ -(O-CH ₂ -CH ₂) _n -
4		71.3			
5		73.1			HO-CH ₂ -CH ₂ -(O-C*H ₂ -CH ₂) _n -
6	179.4	187.8	178.1		HO-CH ₂ -C*H ₂ -(O-CH ₂ -CH ₂) _n - CH ₃ -C*OO-Metal

^a Quoted from the ref 16 for acetic acid (AC) and 1,4-BG. ^b Simulated by ChemDraw (Cambridge Soft Co.) for tetraethylene glycol (TEG).

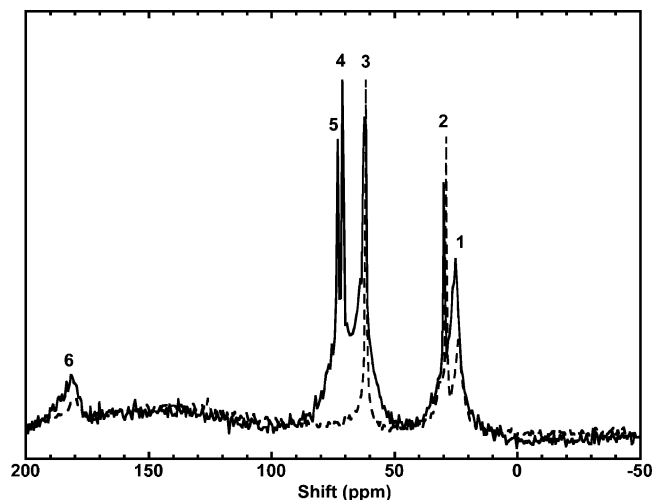


Figure 5. ¹H → ¹³C CP-MAS NMR spectra of samples S(1/0) (dashed line) and S(1/1) (solid line).

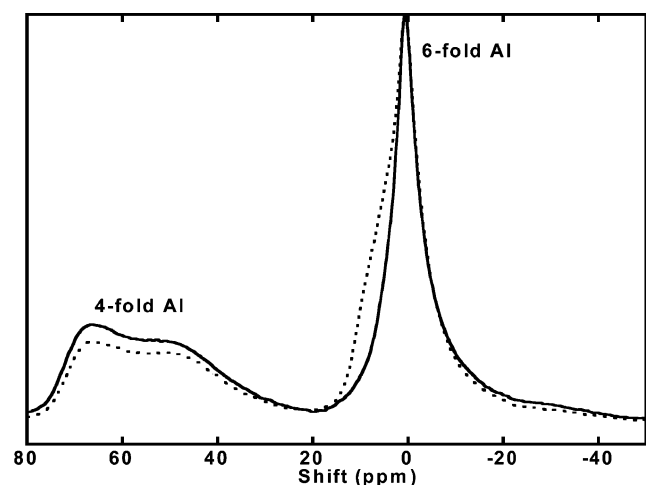


Figure 6. Solid-state ²⁷Al SPE MAS NMR spectra of samples S(1/0) (dashed line) and S(1/1) (solid line).

mentioned increase in the weight loss of TG for sample S(1/1) as well as the FT-IR result.

3.4. Coordination States around Al. The ²⁷Al NMR peaks were observed at 0.6, 50, and 65 ppm in the SPE-MAS spectra of samples S(1/0) and S(1/1), as shown in Figure 6. The peak at around 0.6 ppm is assigned to the 6-fold (octahedral) coordination for Al (Al^{VI}), and the peaks at 50 and 65 ppm are assigned to the 4-fold (tetrahedral) coordination for Al (Al^{IV}). The Al^{VI} peak of sample S(1/1) is sharper than that of sample S(1/0). The integral intensity ratio of Al^{IV} to Al^{VI} for sample S(1/1) was 0.72, being higher than 0.53 for sample S(1/0).

3.5. Photoluminescent Properties. Figure 7 shows the PL and PLE spectra of samples S(1/0) and S(1/1). The excitation peaks were observed at 345 and 450 nm in the PLE spectra of

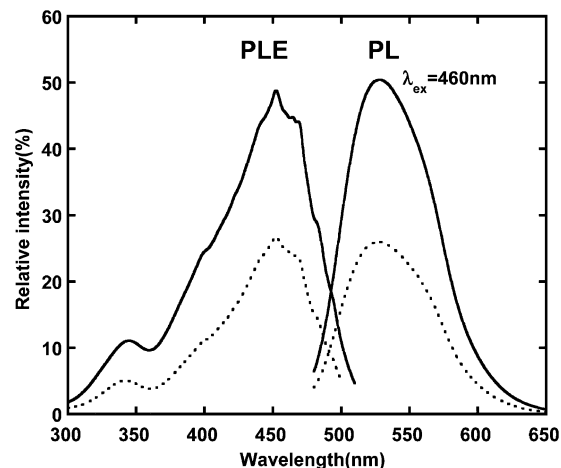


Figure 7. PLE and PL spectra of samples S(1/0) (dashed line) and S(1/1) (solid line).

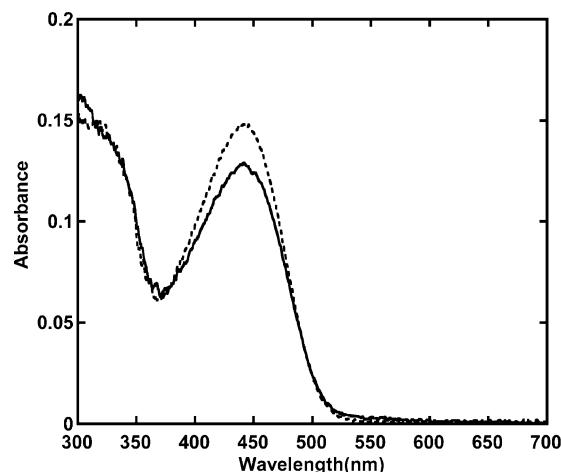


Figure 8. UV-vis absorption spectra of samples S(1/0) (dashed line) and S(1/1) (solid line).

both samples. The emission consisted of a peak at 530 nm and a shoulder at longer wavelength side. The former is assigned to the 5d (²A_{1g}) → 4f (²F_{5/2}) transition and the latter to the 5d (²A_{1g}) → 4f (²F_{7/2}) transition, respectively, for Ce³⁺, since Ce³⁺ with a 4f¹ electron configuration has two ground states of ²F_{5/2} and ²F_{7/2} due to the spin-orbit interaction.¹⁷ The PL intensity of sample S(1/1) was 1.9 times higher than that of sample S(1/0).

The absorption peak was observed at 445 nm in the UV-vis absorption spectra, as shown in Figure 8. Its absorbance of sample S(1/1) was 14% lower than that of sample S(1/0). The internal PL quantum efficiency (IQE) was calculated by the following equation:

$$\frac{\text{IQE}_{\text{sample}}}{\text{IQE}_{\text{ref}}} = \frac{F_{\text{sample}}}{F_{\text{ref}}} \frac{A_{\text{ref}}}{A_{\text{sample}}} \quad (1)$$

where IQE_{ref} is the internal quantum efficiency (72%) of the reference, $(\text{Y}_{2.1}\text{Gd}_{0.9})\text{Al}_5\text{O}_{12}:\text{Ce}^{3+}$, at $\lambda_{\text{ex}} = 470$ nm; F_{sample} , the integral PL intensity of the sample at $\lambda_{\text{ex}} = 460$ nm; F_{ref} , the integral PL intensity of the reference at $\lambda_{\text{ex}} = 470$ nm; A_{sample} , the absorbance of the sample at 460 nm; A_{ref} , the absorbance of the reference at 470 nm. The value of IQE for sample S(1/1) was 37.9%, being higher than 21.3% for sample S(1/0).

4. Discussion

No difference between samples S(1/0) and S(1/1) was observed with respect to the crystallite size, the lattice distortion, and the primary particle size. Therefore, the PL enhancement by addition of PEG cannot be explained in terms of the crystalline and particulate properties. The addition of PEG promotes the incorporation of Ce^{3+} into the YAG nanocrystal according to the compositional analysis. However, the increase in the Ce/(Ce + Y) ratio by a factor of 1.085 by addition of PEG is not enough to explain the increase in the PL intensity by a factor of 1.9 and the increase in IQE by a factor of 1.8.

FT-IR spectra and $^1\text{H} \rightarrow ^{13}\text{C}$ CP-MAS NMR spectra reveal the adsorption of 1,4-BG and PEG on the surface of YAG: Ce^{3+} nanocrystals. The oxygen atoms in 1,4-BG and PEG are probably coordinated to the metallic ions at the surface. As far as one molecule is concerned, PEG has more oxygen atoms in the repeated unit, $-(\text{CH}_2\text{CH}_2\text{O})_n-$, than 1,4-BG. Accordingly, PEG preferentially interacts with the YAG: Ce^{3+} nanocrystal through its multiple coordination sites. This is consistent with the fact that the weight loss up to 700 °C increased from 17.4 to 27.3 wt % by addition of PEG.

It is well-known that surface defects such as dangling bonds act as luminescent killers for the semiconductor nanocrystals.¹⁸ Lu et al. reported that the trap level related with the oxygen vacancy is formed between the ground and excitation energy levels of the luminescent Ce^{3+} center in YAG.¹⁷ Therefore, the surface modification by PEG, i.e., the coordination of oxygen in PEG to the metallic ion, could passivate the oxygen vacancy at the surface of the YAG: Ce^{3+} nanocrystal. This can explain the increase in the IQE value. The surface modification by PEG should also contribute to the prevention of the oxidation from Ce^{3+} to Ce^{4+} during and after the glycothermal synthesis.

On the basis of the crystal structure of YAG, the $\text{Al}^{\text{IV}}/\text{Al}^{\text{VI}}$ ratio is 1.5.¹⁹ The Al^{IV} and Al^{VI} proportions can be estimated by the Al NMR integral intensity ratio of Al^{IV} to Al^{VI} , if a short pulse is used for avoiding the effect due to the large difference in quadrupolar coupling constants between Al^{IV} and Al^{VI} , i.e., for avoiding the selective excitation of the 6-fold coordination Al site.¹¹ In fact, MacKenzie et al. reported that when YAG crystals were obtained by heating the precursor gel at temperatures ranging from 1000 to 1250 °C, the $\text{Al}^{\text{IV}}/\text{Al}^{\text{VI}}$ ratio determined by Al MAS NMR with a 15° pulse became 1.5, being in excellent agreement with the ratio expected from the crystal structure.²⁰ In this work, we used a $\pi/20$ pulse, being shorter than a 15° ($\pi/12$) pulse. The Al NMR integral intensity ratio of Al^{IV} to Al^{VI} increased from 0.53 to 0.72 by addition of PEG. This reveals that the local structural rearrangement around Al^{3+} occurs by PEG modification. The 4-fold and 6-fold

coordination Al sites are adjacent to the 8-fold (dodecahedral) coordination sites of Y^{3+} and Ce^{3+} . The lower proportion of the 4-fold coordination Al site should affect at least the nearest coordination site and would induce the locally distorted structure around Ce^{3+} . This explains the lower PL efficiency of sample S(1/0) by comparison of that of sample S(1/1).

5. Concluding Remarks

The YAG: Ce^{3+} nanocrystal modified by PEG was produced by the glycothermal reaction in the mixture of 1,4-BG and PEG. The surface modification by PEG was confirmed by TG-DTA, FT-IR spectroscopy, and $^1\text{H} \rightarrow ^{13}\text{C}$ CP-MAS NMR. The internal quantum efficiency of the photoluminescence corresponding to the 5d \rightarrow 4f transition of Ce^{3+} in the YAG: Ce^{3+} nanocrystal increased from 21.3 to 37.9% by PEG modification. This increase can be explained by the following items: (i) the surface passivation, (ii) the prevention of the oxidation from Ce^{3+} to Ce^{4+} , (iii) the promotion of the incorporation of Ce^{3+} into the YAG nanocrystal, and (iv) the relaxation of locally distorted structure.

Acknowledgment. We thank Mr. H. Kidera and Dr. M. Nakagawa at Idemitsu Kosan Co., Ltd., for the measurement and valuable discussion of the solid-state NMR data.

References and Notes

- (1) Murota, R.; Kobayashi, T.; Mita, Y. *Jpn. J. Appl. Phys.* **2001**, *41*, L887–L888.
- (2) Wu, X.; Nakua, A.; Cheong, D. *Proc. 10th Int. Display Workshops* **2003**, 1109–1112.
- (3) Kinsman, K. M.; McKittrick, J. J. *Am. Ceram. Soc.* **1994**, *77*, 2866–2872.
- (4) Guo, X.; Sakurai, K. *Jpn. J. Appl. Phys.* **2000**, *39*, 1230–1234.
- (5) Veith, M.; Mathur, S.; Kareiva, A.; Jilavi, M.; Zimmer, M.; Huch, V. *J. Mater. Chem.* **1999**, *9*, 3069–3079.
- (6) Hakuta, Y.; Seino, K.; Ura, H.; Adschiri, T.; Takizawa, H.; Arai, K. *J. Mater. Chem.* **1999**, *9*, 2671–2674.
- (7) Zhang, X.; Liu, H.; He, W.; Wang, J.; Li, X.; Boughton, R. I. *J. Alloys Compd.* **2004**, *372*, 300–303.
- (8) Inoue, M.; Otsu, H.; Kominami, H.; Inui, T. *J. Am. Ceram. Soc.* **1991**, *74*, 1452–1454.
- (9) Inoue, M.; Otsu, H.; Kominami, H.; Inui, T. *J. Alloys Compd.* **1995**, *226*, 146–151.
- (10) Kasuya, R.; Isobe, T.; Kuma, H. *J. Alloys Compd.*, in press.
- (11) Massiot, D.; Bessada, C.; Coutures, J. P.; Taulelle, F. *J. Magn. Reson.* **1990**, *90*, 231–242.
- (12) Inoue, M.; Kimura, M. *Mol. Cryst. Liq. Cryst.* **2000**, *341*, 431–436.
- (13) Yamaguchi, O.; Takeoka, K.; Hirota, K.; Takano, H.; Hayashida, A. *J. Mater. Sci.* **1992**, *27*, 1261–1264.
- (14) Noto, V. D.; Miinchow, V.; Vinadello, M.; Collet, J. C.; Lavina, S. *Macromol. Chem. Phys.* **2002**, *203*, 1211–1227.
- (15) Landry, C. C.; Pappé, N.; Mason, M. R.; Applett, A. W.; Tyler, A. N.; MacInnes, A. N.; Barron, A. R. *J. Mater. Chem.* **1995**, *5*, 331–341.
- (16) Spectral Database for Organic Compounds, SDBS, URL <http://www.aist.go.jp/RIODB/SDBS/>.
- (17) Lu, C.-H.; Hong, H.-C.; Jagannathan, R. *J. Mater. Chem.* **2000**, *8*, 2525–2530.
- (18) Hollingsworth, J. A.; Klimov, V. I. In *Semiconductor and Metal Nanocrystals*; Klimov, V. I., Ed.; Marcel Dekker Inc.: New York, 2004; Chapter 1, pp 1–64.
- (19) Florian, P.; Gervais, M.; Douy, A.; Massiot, D.; Coutures, J.-P. *J. Phys. Chem. B* **2001**, *105*, 379–391.
- (20) Mackenzie, K. J. D.; Kemitt, T. *Thermochim. Acta* **1999**, *325*, 13–18.